ARTICLES

Journal of Semiconductors
(2023) 44, 052201
doi: 10.1088/1674-4926/44/5/052201

Optimizing the morphology of all-polymer solar cells for enhanced photovoltaic performance and thermal stability

Kang An[1, ‡], Wenkai Zhong[2, ‡], Chunguang Zhu[1, ‡], Feng Peng[3], Lei Xu[1], Zhiwei Lin[4], Lei Wang[5], Cheng Zhou[1], Lei Ying[1, †], Ning Li[1, †], and Fei Huang[1]

[1]Institute of Polymer Optoelectronic Materials and Devices, State Key Laboratory of Luminescent Materials and Devices, South China University of Technology, Guangzhou 510640, China

[2]Frontiers Science Center for Transformative Molecules, Center of Hydrogen Science, and School of Chemistry and Chemical Engineering, Shanghai Jiao Tong University, Shanghai 200240, China

[3]South China Institute of Collaborative Innovation, Dongguan 523808, China

[4]South China Advanced Institute for Soft Matter Science and Technology, School of Emergent Soft Matter, South China University of Technology, Guangzhou 510640, China

[5]School of Light Industry and Engineering & State Key Laboratory of Pulp & Paper Engineering, South China University of Technology, Guangzhou 510640, China

Abstract: Due to the complicated film formation kinetics, morphology control remains a major challenge for the development of efficient and stable all-polymer solar cells (all-PSCs). To overcome this obstacle, the sequential deposition method is used to fabricate the photoactive layers of all-PSCs comprising a polymer donor PTzBI-oF and a polymer acceptor PS1. The film morphology can be manipulated by incorporating amounts of a dibenzyl ether additive into the PS1 layer. Detailed morphology investigations by grazing incidence wide-angle X-ray scattering and a transmission electron microscope reveal that the combination merits of sequential deposition and DBE additive can render favorable crystalline properties as well as phase separation for PTzBI-oF:PS1 blends. Consequently, the optimized all-PSCs delivered an enhanced power conversion efficiency (PCE) of 15.21% along with improved carrier extraction and suppressed charge recombination. More importantly, the optimized all-PSCs remain over 90% of their initial PCEs under continuous thermal stress at 65 °C for over 500 h. This work validates that control over microstructure morphology via a sequential deposition process is a promising strategy for fabricating highly efficient and stable all-PSCs.

Key words: morphology; all-polymer solar cells; thermal stability; sequential deposition

Citation: K An, W K Zhong, C G Zhu, F Peng, L Xu, Z W Lin, L Wang, C Zhou, L Ying, N Li, and F Huang, Optimizing the morphology of all-polymer solar cells for enhanced photovoltaic performance and thermal stability[J]. *J. Semicond.*, 2023, 44(5), 052201. https://doi.org/10.1088/1674-4926/44/5/052201

1. Introduction

All-polymer solar cells (all-PSCs), consisting of macromolecular donors and acceptors in the light-harvesting layer, have attracted many broad interests among photovoltaic technologies[1–11]. In addition to the well-established advantages of being light-weight, flexibility, and compatibility with low-cost printing techniques, the photovoltaic performances of all-PSCs have been significantly enhanced by virtue of recently emerged n-type polymers consisting of non-fullerene acceptor (NFA) building blocks in the backbones[12–18]. In comparison to the widely used n-type polymer acceptors, such as N2200, NFA-based n-type polymers exhibited enhanced absorption coefficients that can compensate for the insufficient near infrared (NIR) absorption in NDI-based n-type polymers. Moreover, the gradually tunable energy levels of NFAs allow a wide range of electron-donating polymers for favorable charge transfer and thus improved photovoltaic efficiency[19–22].

It has been established that favorable morphology of the photoactive layer plays a critical role in charge generation and transportation, and thus corresponds to the achievement of high photovoltaic performance as well as device stability[23]. Hence, a wide range of post-treatment processes have been adopted to manage the dynamics of solvent evaporation and film formation for optimized film morphology, such as thermal annealing, solvent vapor annealing after deposition of the bulk-heterojunction (BHJ) photo-active layer[24–26]. Note that the active layer solution containing a small amount of solvent additives, could effectively modify the miscibility and phase purity of relevant components in the corresponding BHJ layer[27]. For all-polymer systems, during the morphological evolution, polymer chains may twist randomly and present complicated morphological dynamics. Thus, it remains a great challenge to achieve favorable morphology of the BHJ films. Alternatively, sequential deposition (SD) methods allow each polymer component to be adjusted and optimized independently, producing a bilayer or pseudo-bilayer active layer to afford a high phase purity and favorable

Kang An, Wenkai Zhong, and Chunguang Zhu contributed equally to this work.

Correspondence to: L Ying, msleiying@scut.edu.cn; N Li, ningli2022@scut.edu.cn

Received 4 DECEMBER 2022; Revised 6 JANUARY 2023.

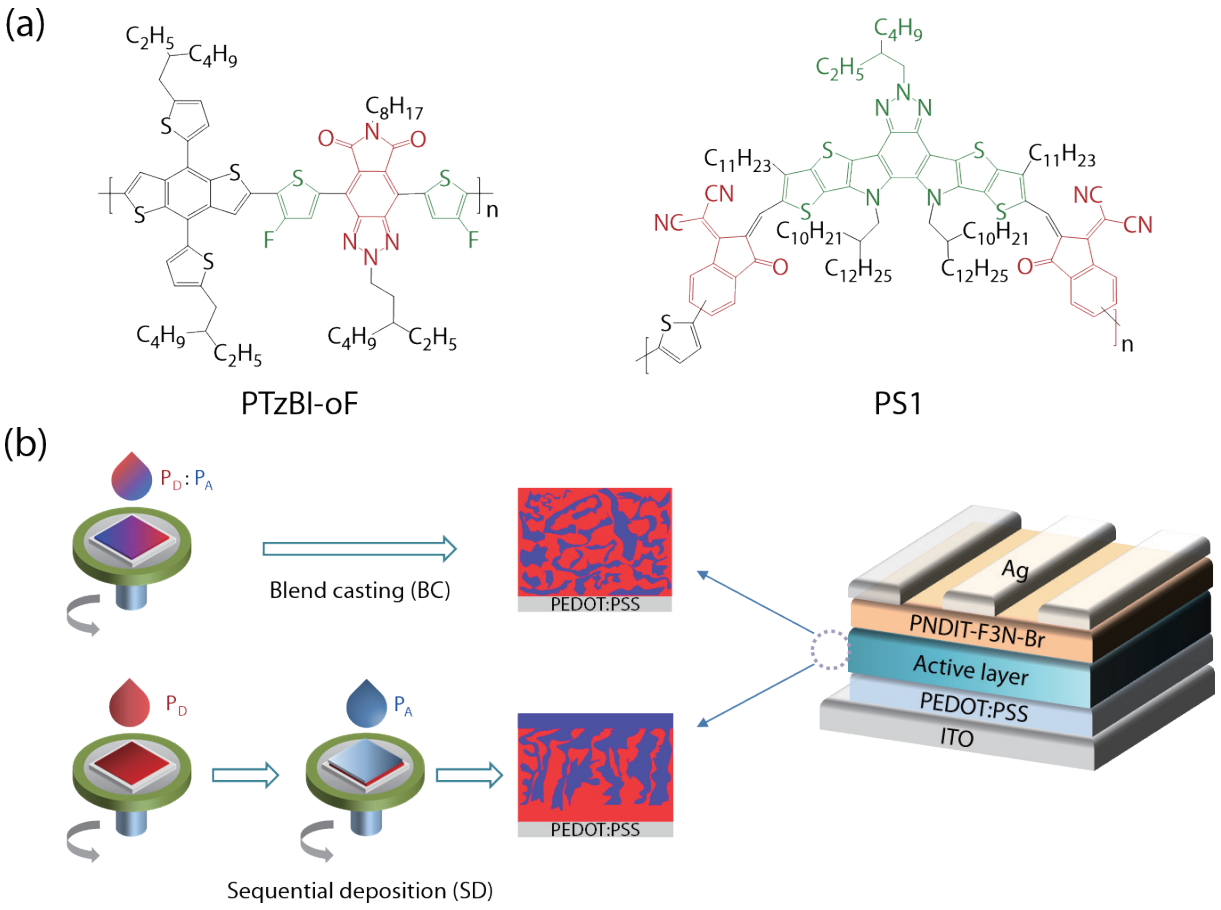

Fig. 1. (Color online) (a) Chemical structures of the polymer donor PTzBI-oF and the polymer acceptor PS1. (b) Schematic diagram of all-PSCs fabricated by the blend casting (BC) and sequential deposition (SD) methods.

phase separations that can facilitate charge transportation and extraction compared to the traditional blend casted (BC) one (Fig. 1)[28, 29]. Moreover, several publications have reported superior stability of SD-processed devices over the corresponding BHJ counterparts[30, 31].

Here we demonstrate that the film morphology can be optimized and the overall performance as well as stability of all-PSCs can be enhanced based on the sequential deposition strategy. The target device consists of a polymer donor PTzBI-oF (including a pyrrolo[3,4-*f*]benzotriazole-5,7(6*H*)-dione moiety) and a polymer acceptor PS1 (containing the NFA Y11 building block), with corresponding molecular structures as shown in Fig. 1(a)[32–34]. Instead of using orthogonal solvents, the PTzBI-oF:PS1 blend films are spin-coated from a chloroform (CF) solution in the presence of a certain amount of dibenzyl ether (DBE) as the solvent additive. The active layer morphology could be manipulated with the DBE additive, leading to an enhanced power conversion efficiency (PCE) over 15%. Detailed morphological investigation revealed that the improved performance of sequentially deposited all-PSCs mainly originated from the formation of favorable crystallinity, crystalline orientation, and phase separation in optimized sequential deposition active layers, which greatly contribute to the suppressed charge recombination and increased charge carrier transport. Meanwhile, the superior long-term thermal stability is achieved in sequential deposition all-PSCs, underlining that the sequential deposition method is a promising approach to further develop all-PSCs with excellent device performance and stability.

2. Results and discussion

2.1. Optical properties

As shown in Fig. 2(a), the absorption spectra of PTzBI-oF with and without DBE are nearly identical. After adding DBE to the PS1 neat film, the absorption coefficient obviously increased to 7×10^4 cm^{-1}. The absorption of the PTzBI-oF film mainly ranged from 500 to 700 nm, which is complementary to the strong absorbance of the low-bandgap polymer acceptor PS1 between 600 to about 900 nm. It is worth noting that the absorption spectra of the photoactive layers processed using either the sequential deposition method or the blend-casting method are nearly identical (Fig. 2(b)). The photoluminescence of PTzBI-oF and PS1 can also be effectively quenched in the photoactive layers processed using the two methods (Fig. 2(c) and 2(d))[35].

2.2. Photovoltaic properties

To evaluate the photovoltaic performance of SD-processed all-PSCs, we fabricated devices with a conventional structure of ITO/PEDOT:PSS/photoactive layer/PNDIT-F3N-Br/Ag[36]. Here, for the SD-deposited photoactive layer, the PTzBI-oF film was spin-coated from CF, followed by depositing PS1 in CF with various DBE contents. For comparison, the optimized PTzBI-oF:PS1 BC all-PSC was also fabricated by spin-coating from a CF:DBE mixed solution. Fig. 3(a) shows the representative current density–voltage (*J*–*V*) curves recor-

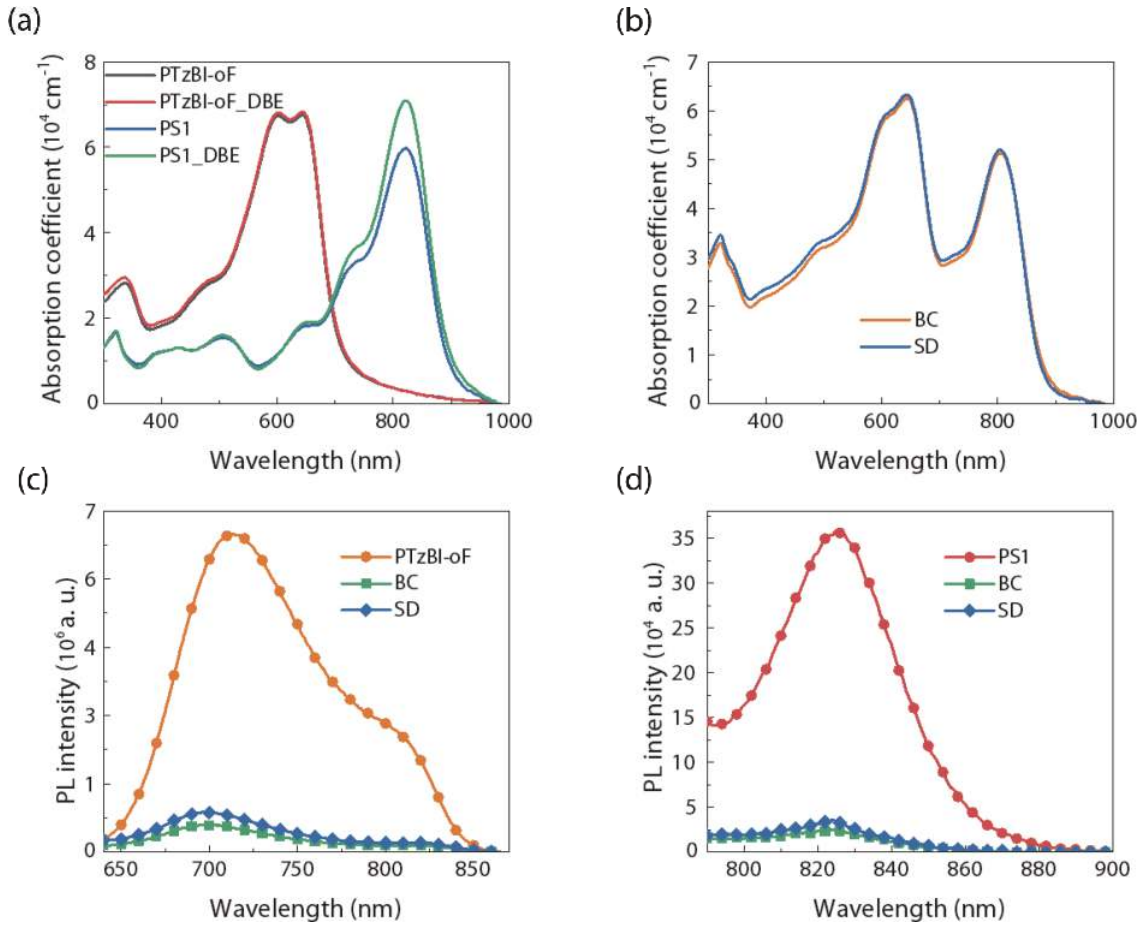

Fig. 2. (Color online) (a) Absorption spectra of neat PTzBI-oF and PS1 films without and with DBE additives. (b) Absorption profiles of blend-casting PTzBI-oF:PS1 and sequentially deposited PTzBI-oF/PS1 blend film. (c, d) Photoluminescent spectra of PTzBI-oF, PS1, blend-casting PTzBI-oF:PS1 and sequentially deposited PTzBI-oF/PS1 film, excited at 620 and 775 nm.

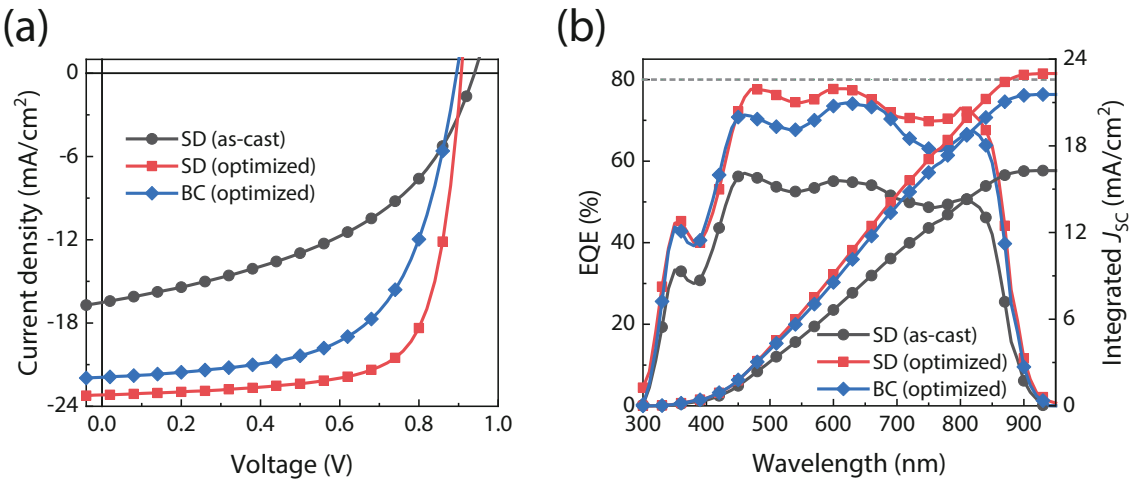

Fig. 3. (Color online) (a) *J*–*V* characteristics, (b) EQE spectra and corresponding integrated J_{SC} curves of sequential deposition and blend casting all-PSCs.

ded under simulated AM 1.5 G illumination with the light intensity of 100 mW/cm^2. The corresponding photovoltaic parameters are summarized in Table 1. The as-fabricated all-PSCs by the sequential deposition method presented a moderate PCE of 7.13%, attributing to the relatively low short-circuit current (J_{SC}) of 16.51 mA/cm^2 and a low fill factor (FF) of 45.94%. However, the efficiency could be significantly enhanced to 15.21% (with an open-circuit voltage, V_{OC}, of 0.906 V, a J_{SC} of 23.18 mA/cm^2 and an FF of 72.35%) by depositing the PS1 layer from the solution containing an optimized ratio of the solvent additive (DBE). The detailed optimization process of SD-processed all-PSCs are summarized in Figs. 1–3. The enhanced J_{SC} of the optimized all-PSCs is consistent with the improved charge carrier mobility, where the hole/electron (μ_h/μ_e) mobility enhanced from $3.22 \times 10^{-4}/4.18 \times 10^{-4}$ to $1.36 \times 10^{-3}/7.31 \times 10^{-4}$ cm^2/(V·s) (Fig. 4). Compared to the control device processed with the BC method (PCE = 12.04%, V_{OC} = 0.895 V, J_{SC} = 21.91 mA/cm^2 and FF = 61.39%), the all-PSCs

Table 1. Photovoltaic parameters of sequential deposition and blend casting all-PSCs.

All-PSCs	V_{OC} (V)	J_{SC} (mA/cm^2)	FF (%)	PCE [a] (%)	$J_{SC,\,EQE}$ [b] (mA/cm^2)
SD	0.94	16.51	45.94	7.13	16.28
(as-cast)	0.94 ± 0.01	16.49 ± 0.20	45.26 ± 1.38	6.90 ± 0.23	
SD	0.91	23.18	72.35	15.21	23.01
(optimized)	0.91 ± 0.01	22.96 ± 0.22	71.67 ± 0.68	14.96 ± 0.25	
BC	0.90	21.91	61.39	12.04	21.55
(optimized)	0.90 ± 0.01	21.78 ± 0.13	60.28 ± 1.11	11.75 ± 0.29	

[a] Average values were obtained from 10 separate devices; [b] Integrated J_{SC} values from the EQE spectra.

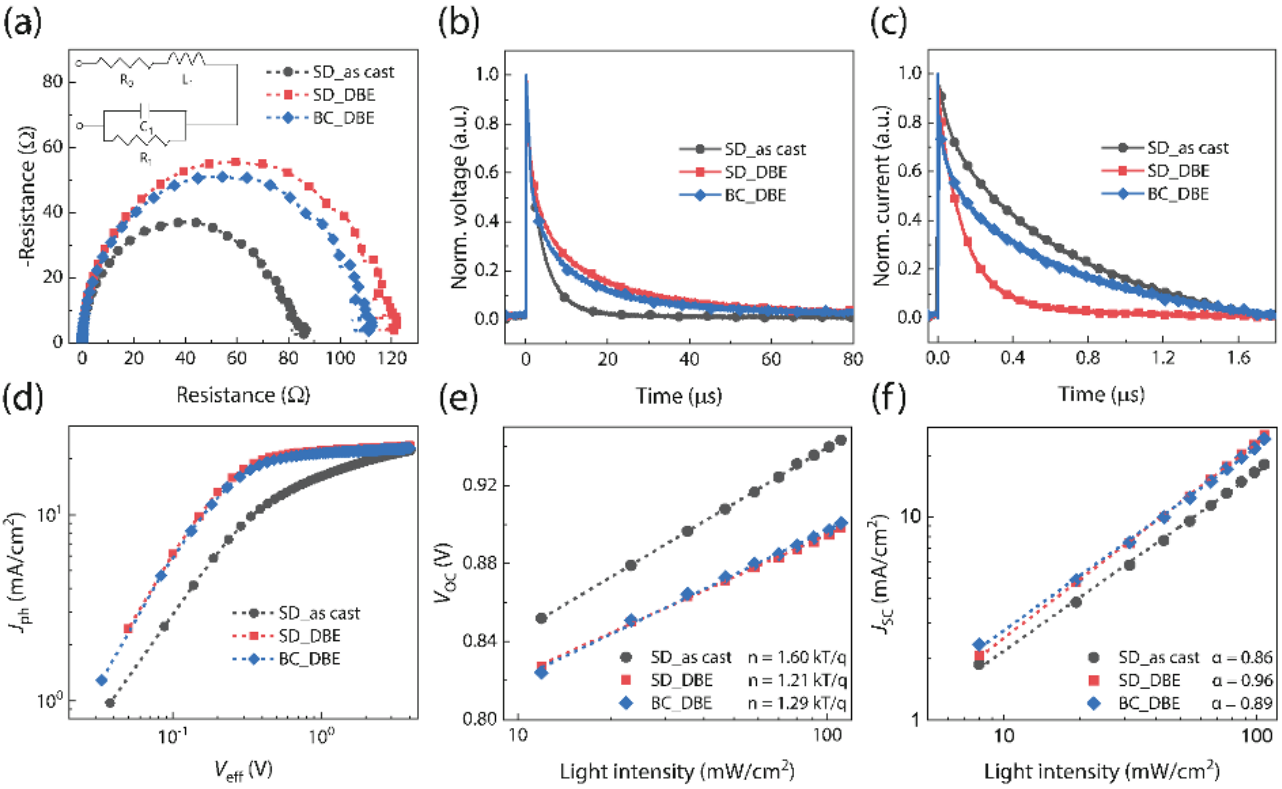

Fig. 4. (Color online) (a) Impedance spectra with the equivalent circuits as inset, (b) normalized transient photovoltage and (c) transient photocurrent curves, (d) J_{ph}–V_{eff} characteristics, (e) dependence of V_{OC} and (f) J_{SC} on light intensity (P_{light}) measurements for PTzBI-oF:PS1 based devices constructed by sequential deposition and blend casting methods.

processed using the SD method showed simultaneously enhanced J_{SC} and FF[37]. The integrated J_{SC} values from the EQE spectra agreed well with those obtained under the solar simulator by *J*–*V* scanning (Fig. 3(b)). The photo-response in the wavelength range of 400–850 nm approaches to 80% for the SD-processed device, illustrating efficient charge dissociation and collection.

2.3. Charge carrier dynamics

The impedance spectroscopy measurement was performed in a dark chamber with the frequency ranging from 20 Hz to 10 MHz (Fig. 4(a))[38]. The dotted lines are the fitting curves with the circuit model shown in the inset, where R_0 represents the series resistance from a number of contacting interfaces, R_1 is the transport and recombination resistances of the active layer. It is noted that, for the optimized sequential deposition devices, R_0 is decreased and R_1 is increased (Table S6), facilitating the charge transport and extraction within the devices. In light of the mitigated recombination in the optimized all-PSCs, we measured the transient photovoltage (TPV) on the corresponding devices[39]. Optimized SD-processed devices showed the decay time of 6.37 μs, which is much longer than that of 3.42 μs for the reference BC-processed device, illustrating retarded charge recombination of the SD-processed device (Fig. 4(b) and Table S6). Moreover, the transient photocurrent (TPC) characteristics of the optimized SD-processed device presented the shortest decay time (τ_{TPC}) of 0.15 μs, which is shorter than the pristine SD-processed without DBE (0.43 μs) and the control device (0.31 μs) processed with the PTzBI-oF:PS1 BHJ blend (Fig. 4(c) and Table S6). This finding indicates more effective charge extraction in the optimized SD-processed device, and is consistent with the improved J_{SC} and FF.

Photocurrent density (J_{ph}) versus the effective voltage (V_{eff}) curves was used to study the effects of the processing methods and DBE additives on the photovoltaic performance of all-PSCs. Here, J_{ph} is defined as the difference between J_L (current densities under illumination) and J_D (current densities under dark); V_{eff} equals to $V_0 - V_{appl}$, where V_0 is the voltage when $J_L = J_D$; and V_{appl} represents the applied voltage bias. As shown in Fig. 4(d), the exciton dissociation probability $P(E,T)$ can be obtained from the ratio of J_{ph}/J_{sat}, where J_{sat} is the saturation photocurrent density. The optim-

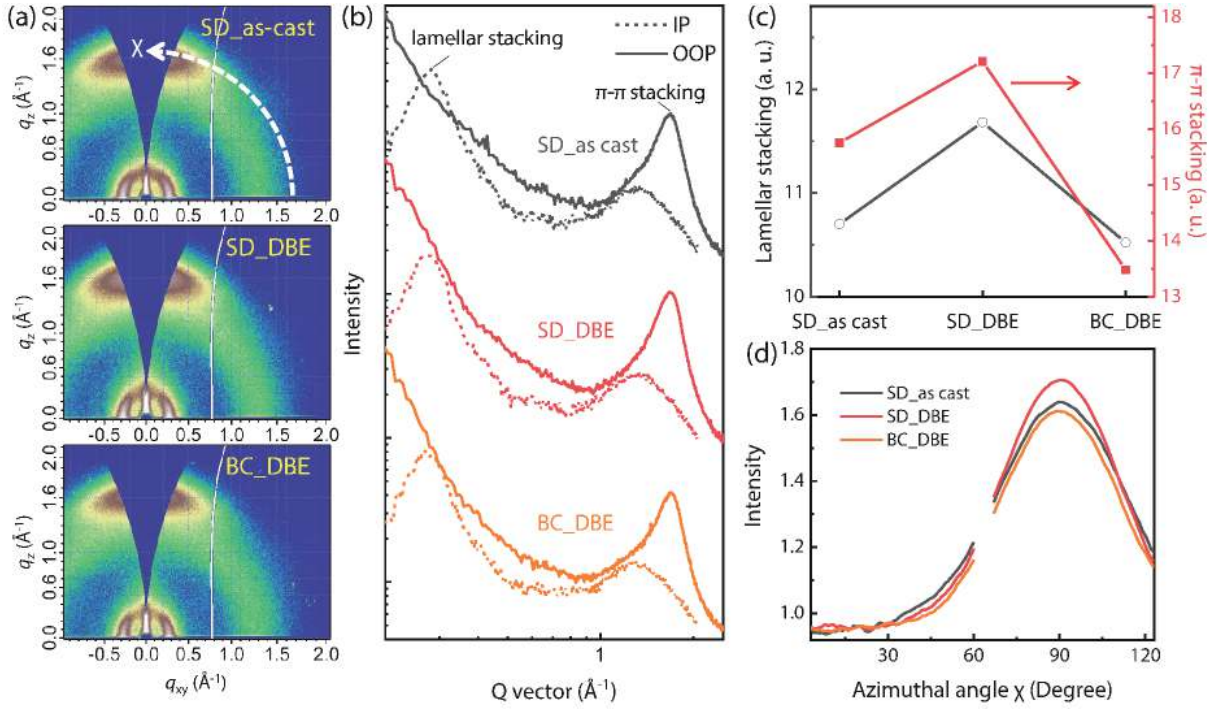

Fig. 5. (Color online) GIWAXS (a) 2D images and (b) sector averaged curves in the IP (dotted lines) and OOP (solid lines) directions. (c) Summary of the peak area of lamellar stacking and π–π stacking reflections. (d) Pole figure of π–π stacking reflections, where the azimuthal angle χ is zero in the q_{xy} direction and 90° in the q_z direction.

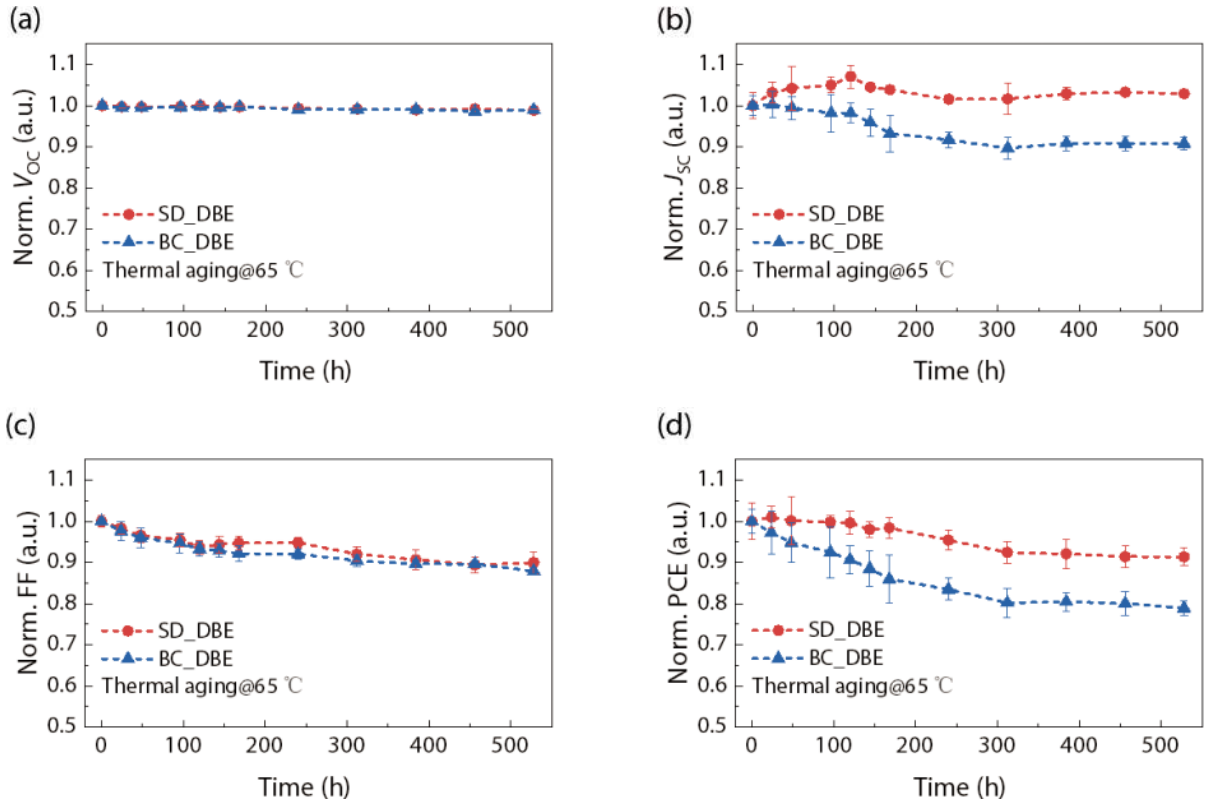

Fig. 6. (Color online) Normalized parameters for optimized PTzBI-oF:PS1 based all-PSCs fabricated by sequential deposition and blend casting methods continuously thermal aging at 65 °C.

ized SD-processed device showed the highest $P(E,T)$ value of 94.18% at short-circuit conditions, which produced a high J_{SC} and FF values (Table S6). Moreover, by analyzing the dependence of V_{OC} and J_{SC} on the decayed light intensity (P_{light}), we observed the weak dependence of V_{OC} on P_{light} for the optimized SD-processed device with a low slope of 1.21 kT/q, while that for as-cast and BC-processed devices are 1.60 kT/q and 1.29 kT/q, respectively (Fig. 4(e)). The slope (α) of J_{SC}–P_{light} plot for the optimized SD-processed device is very close to unity (α = 0.96), while the as-cast SD-processed device and

BC-processed devices showed a linear fitting slope much smaller than unity. The combination of these results indicate that both the Shockley-Read-Hall recombination and the second-order bimolecular recombination are weak in the optimized SD-processed device, which is again consistent with the obtained high J_{SC} and FF[40, 41].

2.4. Film morphology

Grazing incidence wide-angle scattering (GIWAXS) was performed to study the morphological properties of the photoactive blends. Figs. 5(a) and 5(b) depict the scattering images and sector averaged curves in the in-plane (IP) and out-of-plane (OOP) directions. Due to the superposed signals of PTzBI-oF and PS1, the images captured the global crystalline information of the blends[25]. The peak at q ~ 1.69 Å^{-1} in the OOP direction is attributed to the π-π stacking, while the peak at ~0.28 Å^{-1} in the IP direction originates from lamellar stacking. The peak areas were fitted for the evaluation of crystallinity (Figs. 6 and Table S7). For SD-processed blends, the film processed with DBE shows higher intensity for both lamellar and π–π stacking reflections than those of the as-cast film (Fig. 5(c)). For the SD and BC blends processed with DBE, increased peak areas are also resolved for the SD-processed film, where the π-π stacking peak area gains ~28% compared with the BC film. These results indicate that the presence of DBE during film formation promoted the chain-segmental assemblies under prolonged drying process, leading to increased crystallinity of polymers. Such an effect was enhanced when using SD for the film preparation, as SD may provide a crystallization environment with less heterogeneous disruption[42]. The results are in good agreement with the atomic force microscopy (AFM) height images (Fig. S7). For the SD blends, agglomerates due to increased crystallization are observed at the film surface, while the BC film shows fibrillar morphology.

Further analysis was performed by plotting the pole figures for the π–π stacking reflections (Fig. 5(d)). Fitting the pole figures with Gaussian function yields their areas and full-width-half-maximums (FWHMs) (Fig. S8 and Table S8). The areas of the SD-processed films are ~38, higher than the ~34 of the BC film, while the FWHMs of the films processed with DBE are ~48°, narrower than the ~53° of the as-cast film. Thus, the SD processing with DBE not only maximized the crystallinity but also improved the crystalline orientation with increased "face-on" arrangements relative to the substrate. Therefore, the GIWAXS results demonstrate the collective effects of SD and DBE on optimizing the crystalline properties and the favorable phase separation, which is also consistent with the transmission electron microscopy (TEM) images (Fig. S9). The better-developed morphology resulted from the SD processing with DBE is the main reason for the increased charge transport and reduced charge recombination in devices. Thus, substantial improvements in J_{SC} and FF were achieved.

2.5. Thermal stability

Generally, improved crystallinity and "face-on" crystalline orientation of active layers are convinced to inhibit the structural instability[43]. Hence, the unencapsulated all-PSCs fabricated under different conditions were baked in a nitrogen atmosphere to test the long-term stability against thermal stress. Considering the strongly limited device performance for the as-cast all-PSCs, we mainly focused on the stability difference between SD_DBE and BC_DBE all-PSCs. Nevertheless, the stability data for SD_as cast was recorded under the same conditions and provided in Fig. S10. The extremely stable device performance under thermal condition obtained for the SD_as cast devices confirmed the reliability of our test and ruled out the influence caused by the potential degradation of interface layers and other interfered factors, such as chemical and mechanical degeneration. Normalized photovoltaic parameters of SD_DBE and BC_DBE all-PSCs decayed with thermal aging time are shown in Fig. 6. The V_{OC} values of all-PSCs remain stable, while the J_{SC} of BC_DBE devices are visibly degraded in contrast to the robust SD_DBE devices. Both FF of SD_DBE and BC_DBE devices exhibited undesirable degradation, which could be ascribed to the morphological changes at the donor/acceptor interfaces, as reported in the literature[44]. According to these results, the PCE of SD_DBE all-PSCs maintained over 90% of their primeval values under thermal aging at 65 °C for over 500 h. These are very encouraging stability results obtained for highly efficient polymer solar cells with an efficiency over 15%, as the whole device stack including the interface layers and the top electrode was rather stable under thermal stress conditions.

Detailed charge recombination and transportation analysis on SD_DBE and BC_DBE all-PSCs before and after aging were performed. Here, we fabricated large number of devices under the same processing conditions to guarantee the accuracy of our tests. The device performance under the same processing conditions was highly reproducible, so that we could use the fresh and aged devices for a series of characterizations and analyses for comparison. Fig. S11 and Table S6 summarize the charge carrier dynamics measurements for fresh and aged SD_DBE all-PSCs. The slightly decreased R_1 value to 96.30 kΩ after thermal aging can be connected to the influenced charge transport properties, which is also evidenced with the $P(E, T)$ of 92.30%. Moreover, τ_{TPC} was basically unaffected by the thermal aging stress and maintained at about 0.15 μs, suggesting efficient charge extraction. The n values obtained from V_{OC} versus P_{light} measurements was increased to 1.28 kT/q, which displayed trap-assisted recombination in SD_DBE all-PSCs after thermal aging. Hence, the slightly FF degradation originates most probably from the accumulation of charge recombination in SD_DBE devices. To gain deeper insight into the J_{SC} and FF loss for aged BC_DBE devices, charge recombination and transportation analysis were also performed as shown in Fig. S12 and Table S6. The relatively large dropped R_1 value from 71.39 to 55.11 kΩ and quantitative τ_{TPC} and τ_{TPV} values of 0.53 and 1.99 μs indicated charge extraction and transportation were severely affected in aged BC_DBE all-PSCs. Combined with the light intensity dependent V_{OC} and J_{SC}, aged BC all-PSCs may encounter both trap-assisted recombination and bimolecular recombination, leading to faster decreased device performance under thermal stress[45]. Accordingly, we speculate that the improved long-term thermal stability is principally ascribed to the fact that the SD method enables better film morphology and molecular packing, leading to the improved device performance and thermal stability for SD-processed all-PSCs. The long-term light stability of SD_DBE and BC_DBE devices was also evalu-

ated (Fig. S13). The SD_DBE device showed better stability than the BC_DBE one in light soaking conditions.

3. Conclusion

In summary, we showed that the sequential deposition method in combination with solvent additive DBE can produce efficient all-PSCs, reaching a power conversion efficiency of 15.21%. Detailed characterizations revealed that the sequential deposition assisted with the DBE additive played a key role in maximizing the crystallinity, increasing "face-on" arrangements relative to the substrate and regulating phase separation on the mesoscale, thus improving carrier transport and generation, and suppressing charge recombination. Meanwhile, the optimized SD-processed devices delivered an excellent long-term thermal stability at 65 °C. Our contribution further emphasizes the vital importance of controlling the active layer morphology for further development of all-PSCs with excellent device performance as well as device stability.

Acknowledgements

This work was financially supported by Guangdong Major Project of Basic and Applied Basic Research (No. 2019B030302007), and National Key Research and Development Program of China (No. 2019YFA0705900) funded by MOST. N.L. acknowledges the financial support by State Key Lab of Luminescent Materials and Devices, South China University of Technology (Skllmd-2022-03).

Appendix A. Supplementary materials

Supplementary materials to this article can be found online at https://doi.org/10.1088/1674-4926/44/052201.

References

[1] Zhang Z, Li Y. Polymerized small-molecule acceptors for high-performance all-polymer solar cells. Angew Chem Int Edit, 2021, 60, 4422

[2] Kang H, Lee W, Oh J, et al. From fullerene-polymer to all-polymer solar cells: the importance of molecular packing, orientation, and morphology control. Acc Chem Res, 2016, 49, 2424

[3] Zhang D, Fan B, Ying L, et al. Recent progress in thick‐film organic photovoltaic devices: materials, devices, and processing. SusMat, 2021, 1, 4

[4] Zhou N, Facchetti A. Naphthalenediimide (ndi) polymers for all-polymer photovoltaics. Mater Today, 2018, 21, 377

[5] Sun H, Yu H, Shi Y, et al. A narrow-bandgap n-type polymer with an acceptor-acceptor backbone enabling efficient all-polymer solar cells. Adv Mater, 2020, 32, 2004183

[6] Ji X, Xiao Z, Sun H, et al. Polymer acceptors for all-polymer solar cells. J Semicond, 2021, 42, 080202

[7] Shi Y, Ding L. N-type acceptor–acceptor polymer semiconductors. J Semicond, 2021, 42, 100202

[8] Wu B, Yin B, Duan C, et al. All-polymer solar cells. J Semicond, 2021, 42, 080301

[9] Fan Q, Xiao Z, Wang E, et al. Polymer acceptors based on y6 derivatives for all-polymer solar cells. Sci Bull, 2021, 66, 1950

[10] Duan C, Ding L. The new era for organic solar cells: Polymer acceptors. Sci Bull, 2020, 65, 1508

[11] Kong Y, Li Y, Yuan J, et al. Polymerizing small molecular acceptors for efficient all-polymer solar cells. InfoMat, 2022, 4, e12271

[12] Jia B, Wang J, Wu Y, et al. Enhancing the performance of a fused-ring electron acceptor by unidirectional extension. J Am Chem Soc, 2019, 141, 19023

[13] Fan Q, Fu H, Wu Q, et al. Multi-selenophene-containing narrow bandgap polymer acceptors for all-polymer solar cells with over 15% efficiency and high reproducibility. Angew Chem Int Edit, 2021, 60, 15935

[14] Dai S, Li T, Wang W, et al. Enhancing the performance of polymer solar cells via core engineering of nir-absorbing electron acceptors. Adv Mater, 2018, 30, 1706571

[15] Yu Z P, Liu Z X, Chen F X, et al. Simple non-fused electron acceptors for efficient and stable organic solar cells. Nat Commun, 2019, 10, 2152

[16] Fan Q, Ma R, Liu T, et al. High-performance all-polymer solar cells enabled by a novel low bandgap non-fully conjugated polymer acceptor. Sci China Chem, 2021, 64, 1380

[17] Song J, Li Y, Cai Y, et al. Solid additive engineering enables high-efficiency and eco-friendly all-polymer solar cells. Matter, 2022, 5, 4047

[18] Cai Y, Xie C, Li Q, et al. Improved molecular ordering in a ternary blend enables all-polymer solar cells over 18% efficiency. Adv Mater, 2022, 2208165

[19] An K, Peng F, Zhong W, et al. Improving photovoltaic parameters of all-polymer solar cells through integrating two polymeric donors. Sci China Chem, 2021, 64, 2010

[20] Li Z, Ying L, Zhu P, et al. A generic green solvent concept boosting the power conversion efficiency of all-polymer solar cells to 11%. Energy Environ Sci, 2019, 12, 157

[21] Xu X, Li Z, Wang J, et al. High-performance all-polymer solar cells based on fluorinated naphthalene diimide acceptor polymers with fine-tuned crystallinity and enhanced dielectric constants. Nano Energy, 2018, 45, 368

[22] Sun R, Wang W, Yu H, et al. Achieving over 17% efficiency of ternary all-polymer solar cells with two well-compatible polymer acceptors. Joule, 2021, 5, 1548

[23] Zhang X, Yao N, Wang R, et al. On the understanding of energy loss and device fill factor trade-offs in non-fullerene organic solar cells with varied energy levels. Nano Energy, 2020, 75, 105032

[24] Ye L, Cai Y, Li C, et al. Ferrocene as a highly volatile solid additive in non-fullerene organic solar cells with enhanced photovoltaic performance. Energy Environ Sci, 2020, 13, 5117

[25] Zhao F, Wang C, Zhan X. Morphology control in organic solar cells. Adv Energy Mater, 2018, 8, 1703147

[26] Qin Y, Xu Y, Peng Z, et al. Low temperature aggregation transitions in N3 and Y6 acceptors enable double-annealing method that yields hierarchical morphology and superior efficiency in non-fullerene organic solar cells. Adv Funct Mater, 2020, 30, 2005011

[27] Zhong W, Hu Q, Jiang Y, et al. In situ structure characterization in slot-die-printed all-polymer solar cells with efficiency over 9%. Solar RRL, 2019, 3, 1900032

[28] Weng K, Ye L, Zhu L, et al. Optimized active layer morphology toward efficient and polymer batch insensitive organic solar cells. Nat Commun, 2020, 11, 2855

[29] Xu Y, Yuan J, Liang S, et al. Simultaneously improved efficiency and stability in all-polymer solar cells by a p–i–n architecture. ACS Energy Lett, 2019, 4, 2277

[30] Zhang D, Zhong W, Ying L, et al. Overcoming incompatibility of donors and acceptors by constructing planar heterojunction organic solar cells. Nano Energy, 2021, 85, 105957

[31] Wang Y, Zhan X. Layer-by-layer processed organic solar cells. Adv Energy Mater, 2016, 6, 1600414

[32] Peng F, An K, Zhong W, et al. A universal fluorinated polymer acceptor enables all-polymer solar cells with >15% efficiency. ACS Energy Lett, 2020, 5, 3702

[33] Zhu C, Li Z, Zhong W, et al. Constructing a new polymer acceptor enabled non-halogenated solvent-processed all-polymer solar

cell with an efficiency of 13.8%. Chem Commun, 2021, 57, 935
[34] Yuan J, Zhang Y, Zhou L, et al. Single-junction organic solar cell with over 15% efficiency using fused-ring acceptor with electron-deficient core. Joule, 2019, 3, 1140
[35] Li Q, Wang L M, Liu S, et al. Vertical composition distribution and crystallinity regulations enable high-performance polymer solar cells with >17% efficiency. ACS Energy Lett, 2020, 5, 3637
[36] Wu Z, Sun C, Dong S, et al. N-type water/alcohol-soluble naphthalene diimide-based conjugated polymers for high-performance polymer solar cells. J Am Chem Soc, 2016, 138, 2004
[37] Proctor CM, Kuik M, Nguyen T Q. Charge carrier recombination in organic solar cells. Prog Polym Sci, 2013, 38, 1941
[38] Garcia-Belmonte G, Boix P P, Bisquert J, et al. Simultaneous determination of carrier lifetime and electron density-of-states in P3HT: PCBM organic solar cells under illumination by impedance spectroscopy. Sol Energy Mater Sol Cells, 2010, 94, 366
[39] Li Z, Gao F, Greenham NC, et al. Comparison of the operation of polymer/fullerene, polymer/polymer, and polymer/nanocrystal solar cells: A transient photocurrent and photovoltage study. Adv Funct Mater, 2011, 21, 1419
[40] Koster L J A, Mihailetchi V D, Blom PWM. Bimolecular recombination in polymer/fullerene bulk heterojunction solar cells. Appl Phys Lett, 2006, 88, 052104
[41] Etzold F, Howard IA, Mauer R, et al. Ultrafast exciton dissociation followed by nongeminate charge recombination in PCDTBT: PCBM photovoltaic blends. J Am Chem Soc, 2011, 133, 9469
[42] Zhong W, Hu Q, Ying L, et al. Manipulating film morphology of all-polymer solar cells by incorporating polymer compatibilizer. Solar RRL, 2020, 4, 2000148
[43] Du X, Guo J, Min J, et al. Stability of organic solar cells: From fullerene derivatives to non-fullerene acceptors. In: Organic Solar Cells: Materials Design, Technology and Commercialization, 2022, 613
[44] Du X, Heumueller T, Gruber W, et al. Unraveling the microstructure-related device stability for polymer solar cells based on non-fullerene small-molecular acceptors. Adv Mater, 2020, 32, 1908305
[45] Du X, Heumueller T, Gruber W, et al. Efficient polymer solar cells based on non-fullerene acceptors with potential device lifetime approaching 10 years. Joule, 2019, 3, 215

Kang An is a Ph.D. student at the State Key Laboratory of Luminescent Materials and Devices in SCUT. His research focuses on high efficiency and stable polymer solar cells.

Lei Ying received his Ph.D. degree from South China University of Technology (SCUT) in 2009 under the supervision of Prof. Wei Yang. After post-doc research in University of California Santa Barbara with Prof. Guillermo C. Bazan, he joined SCUT in 2013 and was promoted to full professor in 2017. His current interests include developing new organic semiconductors for optoelectronic devices.

Ning Li is a professor at the State Key Laboratory of Luminescent Materials and Devices, South China University of Technology (SCUT). Before joining SCUT, he was a research group leader at Friedrich-Alexander University Erlangen-Nürnberg (FAU) from 2014 to 2021. He received his Ph.D. degree in 2014 under supervision of Prof. Christoph J. Brabec at FAU, Germany. His research interests focus on the development and characterization of solution-processed semiconductors and devices, in particular on the aspects related to the fundamentals and applications of next-generation photovoltaics.